Asymmetric Reconstruction of the Aquareovirus Core at Near-Atomic Resolution and Mechanism of Transcriptional Initiation

Alexander Stevens[1,2,3,#], Yanxiang Cui[2,#], Sakar Shivakoti[1,#], Z. Hong Zhou[1,2,*]

[1]Department of Microbiology, Immunology and Molecular Genetics, University of California, Los Angeles (UCLA), Los Angeles, California 90095, USA

[2]California NanoSystems Institute, UCLA, Los Angeles, California 90095, USA

[3]Graduate program of biochemistry and molecular biology, UCLA, Los Angeles, California 90095, USA

[#] Contributed equally

*To whom correspondence should be addressed

Phone: 310-694-7527, Fax: 310-206-5365; E-mail: Hong.Zhou@UCLA.edu

Abstract

The *Reoviridae* family of dsRNA viruses is characterized by its capacity for endogenous transcription of multipartite genomes within proteinaceous capsids of 1 to 3 layers. These viruses share an inner core particle (ICP) which conforms to icosahedral, T=2*, symmetry, but differ in two major aspects: first, the presence or absence of RNA-capping turrets; second, the number of additional host-specific capsid layers that are often lost upon cell entry. While the role of these additional layers in host infection is generally understood, the absence of asymmetric ICP structures from multilayered reoviruses has obfuscated our understanding on the impact of successive removal of these external layers on the structural organization of the inner capsid and its effect on transcription initiation. Here, we present the 3.4 Å resolution structure of the aquareovirus (ARV) ICP, and atomic models of the capsid shell proteins VP3 and VP6, the transcriptional enzymatic complexes (TECs) VP2 and VP4, and RNA-capping turret protein VP1. These structures reveal significant differences when compared to previously determined, coated ARV structures and the single layered cytoplasmic polyhedrosis virus (CPV). Compared to the ARV virion and infectious subvirion particle (ISVP) structures, the ARV ICP undergoes significant capsid expansion and widening of the TEC's and turret's nucleotide processing channels. In contrast to CPV which relies solely on allosteric regulation by binding transcriptional cofactors, these conformational changes suggest the loss of outer capsid layers may regulate transcription initiation in ARV. These results shed new light on the mechanism of transcription initiation amongst turreted, multilayered members of *Reoviridae*.

Introduction

The *Reoviridae* family of double stranded RNA (dsRNA) viruses, consists of 15 genera differentiated by the number of protein layers composing the capsids and the presence (*Spinareovirinae* subfamily, 9 genera) or absence (*Sedoreovirinae* subfamily, 6 genera) of turrets along the innermost layer and whose members include the diarrhea causing rotavirus which causes about 440,000 deaths in young children annually (Parashar et al., 2003). Both *Sedo-* and *Spinareovirinae* enclose their segmented dsRNA genomes within non-enveloped proteinaceous shells, or capsids, of one to three layers. Regardless of number of genome segments or capsid layers however, the innermost layer from both subfamilies is an icosahedral, T=2*, inner capsid particle (ICP) without exception. During infection, reoviruses shed their outer layers while the ICP remains intact to evade the host's viral genome detection machinery, and act as a nanomachine to endogenously transcribe positive-sense viral messenger RNA (mRNA) at transcriptional enzymatic complexes (TECs) along the capsid lumen (Cui et al., 2019; Skehel & Joklik, 1969). Capping enzymes furnish the newly synthesized viral mRNA with 5' caps upon export to prevent exonucleolytic degradation and enable ribosomal translation (Decroly et al., 2012).

Whilst the inner capsid core in the *Sedoreovirinae* subfamily members such as blue tongue virus (BTV) and rotavirus is generally smooth, each vertex of the *Spinareovirinae* subfamily members such as cytoplasmic polyhedrosis virus (CPV) and aquareovirus (ARV) are decorated by pentameric turrets which surround each fivefold icosahedral (I5) vertex of the ICP (King et al., 2012). These turrets are pentamers of multi-enzyme complex that caps the 5' ends of cytosol-bound viral mRNA as it travels out along the 5-fold axis from a transcribing ICP (Luongo et al., 2000). This differs from *Sedoreovirinae* members where the in-situ mRNA capping location remains a subject of speculation (Kumar et al., 2020). This process is well

understood for members of the *Spinareovirinae* (Cheng et al., 2008; Cheng et al., 2011; He et al., 2019; Zhang et al., 2005; Zhang et al., 2010)

Among viruses of the *Spinareovirinae* subfamily, cytoplasmic polyhedrosis virus (CPV, a member of the cypovirus genus) is the simplest, structurally, having a single-layered capsid that is equivalent to the ICP of double- or triple-layered members of *Reoviridae*. Owing to its simpler structural organization, CPV has long served as a model to study the life cycle of turreted reoviruses. When presented a susceptible cell, a quiescent CPV virion enters via endocytosis. Upon cell entry, the CPV TPs bind S-adenosyl methionine (SAM) and adenosine triphosphate (ATP), inducing limited capsid expansion along with other capsid alterations thought to facilitate genome transcription (Yang et al., 2012; Yu et al., 2015; Zhang et al., 2022). In the transcribing state, viral RNA-dependent RNA polymerases (RdRps), along with nucleotide triphosphatases (NTPases), transcribe viral mRNA, which receives its 5' cap from the turrets en route to the cytosol where they utilize the host's translational machinery.

However, the single-layered architecture that makes CPV an attractive model system also renders it an inadequate model of the numerous, multi-layered, reoviruses. The additional capsid layers of other *Spinareovirinae* members such as the double-layered aquareoviruses may inhibit the same architectural changes to the inner capsid observed in CPV (Yang et al., 2012; Yu et al., 2015; Zhang et al., 2022). Endemic aquareovirus in North America and China causes hemorrhagic diseases in golden shiner and grass carp, respectively (Fang et al., 2005; Nason et al., 2000); and their cryoEM structures of the American and Chinse aquareovirus virion isolates have been resolved to 22 and 3 Å resolution, respectively (Ding et al., 2018; Shaw et al., 1996; Wang et al., 2018). These double-layered structures of ARV are highly similar to that of the Orthorevirius virion (Dryden et al., 1993; Pan et al., 2021), but are distinct from that of CPV or BTV. The presence of a second layer gives ARVs an additional life stage between the quiescent and transcribing stages known as the primed state, which involves a

more complicated array of structural changes and outer layer removal to prepare the virus for transcription (Ding et al., 2018). The outer layer of ARV capsids are comprised of small VP7 protection proteins and large VP5 penetration proteins, the former of which is extracellularly cleaved, exposing VP5 and creating a maximally infectious form of ARV known as the infectious subvirion particle (ISVP) (Nason et al., 2000), which uses its newly exposed VP5 penetration proteins to escape the endocytic pathway and deposit the transcriptionally competent ICP to the host cytosol (Zhang et al., 2010) (Fig. S1). Like other dsRNA viruses, ARVs contain transcriptionally competent inner capsid particles (ICP) or cores, which remain intact following the shedding of the penetration protein (Kim et al., 2004; Nason et al., 2000; Skehel & Joklik, 1969). From the cytosol the ICP can simultaneously synthesize and export viral mRNA from all genome segments and append 5' methylated guanosine caps to the nascent mRNA. This T=2* icosahedral core is composed of 120 copies of the VP3 capsid shell protein (CSP) and an equal number of VP6 clamp proteins which protect the 11 dsRNA segments and their equivalent number transcriptional enzymatic complexes (TECs) each composed of VP2 and VP4. To date, only the asymmetric structures of complete ARV virions and ISVPs have been resolved to high-resolution, thus it is unclear what, if any, structural changes occur within the ICP during uncoating (Ding et al., 2018; Wang et al., 2018).

Asymmetric sub-particle reconstruction methods coupled with iterative symmetric relaxation workflows have enabled visualization of the asymmetrically attached RdRp and NTPase inside the core of several dsRNA viruses (Cui et al., 2019; Ding et al., 2018; Zhang et al., 2015). However, no asymmetric reconstructions of ICPs from turreted, multi-layered reoviruses are available to describe the conformational changes undergone by the ICPs. Consequently, whether the external layers of the multi-layered turreted dsRNA viruses also play a structural and functional role in transcription in addition to their involvement in cell entry is not known in the absence of a structure for comparison of ICPs to virions.

In this study, we report the first asymmetric structures of an ICP originating from a multilayered reovirus from the *Spinareovirinae* subfamily by cryo-electron microscopy (cryoEM). Through comparison with existing multilayered ARV structures our work reveals subtle architectural changes between the coated and uncoated ARV core particles which presumably facilitate endogenous transcription. These changes yield a particle with significantly increased internal volume and widened turret exit channel. Our structure also enabled modeling of previously unresolved TEC and CSP segments, which illustrate the interactions between the CSP N-termini, the TEC, and the adjacent genomic RNA absent the protective VP7-VP5 layer. As the first high-resolution asymmetric structure of the innermost core of a multi-layered member of the *Spinareovirinae* subfamily of the *Reoviridae*, this structure fills in a knowledge gap in the ever-growing repertoire of asymmetric reconstructions of dsRNA viruses, demonstrating the conformational difference between coated and uncoated reoviruses.

Results and Discussion

Asymmetric reconstruction of GSRV core resolving 11 TEC-occupying and 1 RNA-filled vertices

We determined the asymmetric structure of the GSRV ICP by following a sequential symmetry relaxation approach as described previously (Ding et al., 2018; Zhang et al., 2015). Virus structures were initially refined with icosahedral symmetry imposed and finer details unique to regions were resolved via symmetry expansion and focused classification as detailed in previous works (Ding et al., 2018; Pan et al., 2021) (Materials and Methods). With this, four asymmetric structures were obtained: three from the 5-fold symmetrical vertices, which include the polar vertices at 3.5 Å and the tropical vertices with and without the TECs to 3.4 Å and 3.7 Å respectively, and structures of the and a reconstruction of the complete capsid featuring 11 TECs at 4.1 Å. The resolution of TEC containing sub-particles following averaging of equivalent

copies reached 3.4 Å. Our asymmetric reconstruction of the GSRV core contains 60 VP1 turret proteins, 120 VP3 capsid shell proteins (CSPs), 120 VP6 clamp proteins, 11 TECs under 12 vertices, with only one southern tropical vertex lacking a TEC complex (Fig. 1F).

These 11 TECs within GSRV core are internally organized following pseudo-D_{3d} symmetry, with 6 TECs occupying the icosahedron's poles while 5 are situated along the equatorial plane at the northern and southern tropics (Fig. 1D). 11 dsRNA segments between 0.8 and 3.9 kbps compose the GSRV genome and are tightly packaged inside the capsid (Fig. 1C); the outermost dsRNA layer shows large, persistent, parallel lengths for each RNA double-strand, with an average of 27 Å between neighboring strands, consistent with the previous ARV structures, despite the increased internal capsid volume (Fig. 1B-C) (Ding et al., 2018).

Loss of outer coat proteins leads to expansion of ICP capsid

Lacking the outer capsid proteins VP5 and VP7, the ARV ICP retains the icosahedral, T=2*, inner capsid shell composed of 60 asymmetric dimers of the 1,214-residue, wedge-shaped VP3 capsid shell proteins (CSPs) and 120 symmetrically arranged copies of the clamp protein (VP6) (Fig. 1A). Consistent with the previously resolved ARV capsid structures, VP3 dimers ($VP3_A$ and $VP3_B$) encircle each 5-fold vertex; with $VP3_A$ conformers seated around the 5-fold vertex center, creating pores adjacent to each TEC's template exit channel for direct transcript capping and release via VP1 turret proteins (TPs) (Fig. 1C-D). $VP3_B$ conformers partially intercalate between $VP3_A$ monomers, and form 3-fold vertices with neighboring decameric assemblies (Fig. 1D). Absent conspicuous CSP rearrangements, the internal volume of the ICP increased by about 9.3% relative to the previously resolved GCRV virion and ISVP with which GSRV shares 96-100% a.a. sequence identity (Ding et al., 2018; McEntire et al., 2003; Wang et al., 2018). The motion undergone by individual decamers includes a 10 Å rise away from the virion origin and subtle expansion of the CSPs (Movie S1) (Goddard et al., 2018). The observed expansion can

be attributed to a non-uniform elongation of the VP3 dimers ~6 Å radially from the I5 vertices relative to their coated counterparts and creates an expanding and rising motion around the decameric subunit (Movie S1,3). Motion isn't uniform across the VP3 monomers however, and even differs between VP3 conformers.

Per historic naming conventions, each ARV CSP is divided into three distinct domains. Extending radially from the I5 vertices, these domains include the α-helix rich apical "tip" nearest the I5 vertices (a.a 486-830), the large carapace domain (a.a. 190-485, 831-976, and 1144-1214), and the small β-sheet rich dimerization domains (a.a. 977-1143) (Fig 1D). The local motion of CSP dimers (Movie S2) reveal a non-uniform elongation of the apical and carapace domains, with the alpha helices moving radially away from the I5 vertices and towards the icosahedral two-fold and three-fold (I2 and I3) vertices for $VP3_A$ and $VP3_B$ respectively (Movie S2). In the apical domain helices 13 and 14 and their conjoining loop (a.a. 490-518), which line the I5 transcript exit channel at the luminal side of the capsid, are largely unperturbed by the capsid shifts and maintain a consistent pore diameter. By contrast I5 adjacent external elements along the capsid move outward and away from the I5 channel, and homologous helices 13 and 14 of $VP3_{\underline{B}}$ expand in a similar manner to the rest of the apical domain. Closer inspection reveals strong conservation of $VP3_A$ residues adjacent to the I5 pore (VP3 a.a. RMSD .464 Å) when compared to the quiescent virion and ISVP structures (Ding et al., 2018; Wang et al., 2018). Despite exhibiting outward motion, the secondary structural elements of CSPs which interface with the clamp and turret proteins interfaces appear to move as rigid bodies, presumably constrained by interactions with the essential clamp and turret proteins (Movie. S2).

Despite migrating away from the I5 vertices the global architecture and CSP contacts of clamp proteins remain consistent when ICP and virion clamp proteins are superimposed (RMSD 0.667 Å). Thus, VP6 conformer changes can be summarized as lateral shifts of 4-5 Å away from the I5 vertices, with no apparent conformational changes. As the clamp protein VP6 mediates

inner-outer capsid protein (VP3-VP5) interactions, this may provide the platform on which the VP5 layer can bind to and compresses the inner layer in virion particles. In keeping with this, previous studies have demonstrated that reovirus ICPs can be recoated supporting the notion that these ICP VP6 structures are capable of VP5 association (Farsetta et al., 2000).

Capsid expansion leads to subtle TEC rearrangements

Several dsRNA segments interact with each TEC and these interactions stabilize the genomic segments enabling improved visualization of their major and minor grooves within the ARV ICP as observed in other RNA viruses (Fig. 2A) (Dai et al., 2017; Pan et al., 2021). 5 major dsRNA segments are observed adjacent to each TEC and are labeled “Front Bottom,” “Bound,” “Front Top,” “Rear Top,” and “Rear Bottom” RNA segments based on their positions relative to the TEC (Fig. 2A). At the polar TECs a 6th RNA molecule is observed adjacent to the TEC template entrance, labeled “Terminal” (Fig. 2B). Consistent with previous ARV structures, VP2 is a 1274-residue RNA-dependent RNA polymerase (RdRp) which, like CPV RdRp VP2, is organized into three major domains—N-terminal domain (1-387), C-terminal bracelet (902-1274), which sandwich the RdRp core (388-901), and are further differentiated into the thumb (793-901), fingers (388-557 and 595-690), and palm (558-594 and 691-792) subdomains (Fig. 2B-C) (Ding et al., 2018; Wang et al., 2018). The fingers house the NTP entry channel and, with the thumb, assist in elongation and proofreading while the palm catalyzes phosphodiester bond formation between new NTPs and the growing strand via D591, D740, and D741, all three of which appear in beta sheets and are highly conserved in reovirus RdRp (Fig. 2C) The N- and C-terminal domains are multifaced: In addition to shielding the RdRp core from any internal environmental changes, they bind dsRNA and other viral core proteins (Fig. 3B,H). Consistent with our previous findings, the C-terminal bracelet of this non-transcribing ICP does not occlude the template exit channel as it does in quiescent CPV (Fig. 2G) (Ding et al., 2018). As

previously observed, the polymerase possesses several channels to funnel RNA template and products down differing paths (Movie S3) (Parker et al., 2002).

Our RdRp structure reveals several local architectural changes within these transcriptional channels when compared to structures form the ARV ISVP (Fig 2D-E, and Movie S3). When viewed down the template entry channel we observe a positively charged Finger domain loop (a.a.s 520-535) moves out of the template entry channel from the ISVP to ICP, widening the channel for template entry (Fig. 2E, Movie S3). From within the channel, we observe the priming loop (a.a. 560-572), thought to separate template and transcript strands, moves away from the transcript exit channel and orients the catalytically important S267 residue towards the incoming template (Fig. 2 F, Movie S3). This migration away from the bracelet domain widens the mRNA exit channel, likely promoting exit towards the adjacent I5 pores. From the external TEC view, we also observe an RdRp expansion along the capsid lumen, is linked to the radial expansion of the capsid beneath it (Movie S3). This contrasts with the VP4 NTPase which undergoes a unidirectional shift, consistent with the radial expansion of the capsid. These movements may be linked to the asymmetric association of the TEC along the expanding decameric subunit. As the NTPase is situated primarily atop the $VP3_1$ dimer it moves along with the $VP3_1$ dimer elongation, whereas the RdRp, which is seated across $VP3_{1\text{-}4}$, is seemingly drawn in several directions based on the expansion of the capsid and the proportion of RdRp associated with each conformer pair (Fig. 3A). As uncoating is necessary to synthesize complete viral transcripts, the subtle conformational changes in the TECs observed here may be essential to carrying out efficient viral transcription.

CSP VP3 and NTPase VP4 N-termini interact with replicative machinery

In the asymmetrically reconstructed sub-particles, several previously unmodeled flexible regions of the RNA-binding domain in TEC NTPase are resolved alongside the Zn-finger containing N-

terminal domains of VP3 CSPs each of which exhibit interactions with the viral genome (Fig. 3). We will first describe the newly resolved N-terminal region of the ARV NTPase.

Viral TECs are situated beneath 11 of the 12 I5 vertices in ARV, containing one RdRp and accompanying NTPase molecule per TEC (Fig. 1E). We previously reported the structure of the ARV NTPase, revealing three distinct domains: the N-terminal RNA-binding domain (RBD, a.a. 1-285), the NTPase domain (a.a. 286-602), and the C-terminal domain (CTD a.a. 603-718) (Ding et al., 2018). The NTPase RBD is composed of two subdomains, the 'tip' (a.a. 80-123) and 'main' (a.a. 1-79 and 124-285) which differ based on their electrostatic potentials and are separated by a neutral crevasse (Fig. S3). In the previous structure, the *tip* domain was entirely unresolved along with a large portion of the *main* domain (a.a. 73-189) (Fig S3). In our structures we observe these previously missing NTPase segments extend away from the stable, globular TEC complex. This flexibility may help accommodate dynamic RNA interactions throughout transcription. The newly modeled N-terminal residues reveal a flexible region homologous to that of ARV's mammalian reovirus (MRV) cousin but of a distinct fold (Pan et al., 2021), exhibiting limited RdRp contacts but extensive genome interactions (Fig 2I-J).

Previously, the N-terminal residues of $VP3_A$ conformers were shown to associate with and lie along the exterior of the TEC, on both the RdRp and NTPase (Ding et al., 2018), and were suggested to anchor the TEC into place. The N-terminal region of ARV and MRV CSPs are also thought responsible for binding dsRNA during virus assembly (Lemay & Danis, 1994). The newly modeled $VP3_A$ N-terminal residues include the previously unresolved residues 108-152 ($VP3_{A1-4}$) which contain previously identified Zn-finger domains (a.a. 116-141) (Fig 3C-G), and conform to a traditional Cys_2His_2 motif, known to bind nucleotides (Fig 3E). Previous reporting suggests that the N-terminal Zn-fingers of MRV CSPs are unnecessary for dsRNA binding, and instead mediate stability of the capsid, despite demonstrated nucleotide binding affinity (Lemay & Danis, 1994; McDonald & Patton, 2011; Yu et al., 2011). In keeping with this

we observe the four newly resolved Zn-fingers ($VP3_{A1-4}$) lie along the TEC, with $VP3_{A2-4}$ situated along an RdRp cleft opposite the NTPase, and $VP3_{A1}$ seated along the VP4 NTPase domain forming a four-pronged setting that anchors the TEC complex to the capsid shell (Fig 3D). The $VP3_{A5}$ N-terminus also extends towards the RdRp, however we were unable to resolve the Zinc finger in either sub-particle reconstruction. We also observe that at both the tropical and polar vertices the $VP3_{A3}$ Zn-finger contacts the rear bottom genome segment (Fig 3E-F). This observation suggests these N-terminal Zn-fingers may help to regulated transcription initiation as previously observed in rotavirus (Ding et al., 2019). It may be the case therefore that ARV VP3s are multifunctional, promoting TEC assembly and stability while maintaining genome organization in the quiescent particles. Despite the significant conformational changes of the capsid exterior, the Zn-fingers appear in positions consistent with the low resolution ISVP structures, suggesting that the Zn-fingers may function independently. This may be enabled by the flexible linker within the of the CSP N-terminal domains (a.a. 140-190), which extend slightly to accommodate the capsid expansion, while maintaining their TEC positioning without influencing the genome organization of transcription state (Movie S3).

Structure of the ICP turret protein VP1, a multi-enzyme complex

Atop each I5 vertex of GSRV sits a pentameric turret composed of 5 copies of VP1 TPs (Fig 1A & 4A). These pentameric turrets form axial channels atop the pores through which the genome is translocated and provides mRNA capping functionality (Reinisch et al., 2000). CPV and MRV virions both have spike proteins which occupy the turret channel and serve dual roles, mediating cell entry, and occluding the mRNA exit channel to prevent premature transcript escape (Figure 4A) (Pan et al., 2021; Zhang et al., 2022).

ARVs lack a spike homologue therefore it is unclear how they might prevent premature transcript escape. Like MRV, ARV TPs are composed of 5 distinct domains: the GTase (a.a. 2-390), a bridge domain (a.a. 391-438, 695-806), MTase I (439-694) MTase II (807-1029), and

Flap (1030-1298) containing 3 immunoglobulin-like (IG) folds, two of which extend to cover the axial channel (Fig 4C). When ICP and virion turrets are compared we observe a significant axial extension of the ARV turrets and widening of the turret channels (Fig. 4B-C). Local alignment of the 5 TP domains reveals that the enzymatic GTase and MTase domains remain stable (RMSD 0.842 Å and 0.907 respectively) while domain separation occurs at the flexible linker regions (a.a. 391-438, 695-806) between the GTase, MTase, and flap domains. This separation is enabled by the loss of the outer coat protein VP5 that would otherwise clash with the new TP architecture (Fig 4A). As ARV lacks a spike protein homologue, we investigated the flap domains that line the turret exit channel. When local alignment is performed it is clear there are significant conformational changes within the domain (Fig. 4 D). This difference is caused by the movement of the two C-terminal IG domains moving at the flexible linker region (a.a. 1129), which undergoes an outward shift of 14 Å and counterclockwise twist when viewed from within the I5 channel (Fig. 4D). This finding, coupled with the changes to capsid and TEC architecture, suggest a regulatory mechanism of transcription wherein the uncoating of ARV yields a particle whose capsid better accommodates genome transcription and whose capping enzymes are widened for transcript export.

Conclusions

This work provides the first near-atomic asymmetric reconstruction of an ICP from a turreted, multilayered reovirus particle which exhibits subtle but functionally important conformational changes compared to coated ARV structures. These changes in the internal capsid volume, along-side a widening of TEC nucleotide channels and extension of the 5’-cap synthesizing turret proteins create the architectural environment conducive to endogenous transcription. As the ICP genome remains in the quiescent state, it is conceivable that transcription initiation requires factors such as S-adenosyl methionine and NTPs in addition the conformational changes observed here. In this manner, the highly specialized outer capsid layers serve as a

useful transcriptional regulator, ensuring that transcription requires not only the presence of cofactors, but also loss of outer capsid layers which occurs upon cell entry.

Acknowledgements

This work was supported in part by grants from the National Institutes of Health (AI094386 to Z.H.Z.). A.S. received support from NIH Ruth L. Kirschtein National Research Service Award AI007323. We acknowledge the use of resource at the Electron Imaging Center for Nanomachines supported by UCLA and by instrumentation grants from NIH (1S10RR23057, 1S10OD018111 and U24GM116792) and NSF (DBI-1338135 and DMR-1548924). We acknowledge support from the UCLA AIDS Institute, the James B. Pendleton Charitable Trust and the McCarthy Family Foundation.

Author contributions

Z.H.Z. designed and supervised the project; S.S. prepared sample and made cryoEM grids; Y.C. performed cryoEM imaging and 3D reconstruction; A.S. built the atomic models, interpreted the structures, made the figures and wrote the paper with input from Z.H.Z.; All authors reviewed and approved the paper.

Conflict of interest. The authors declare no competing interests.

Methods and Data Availability

Viral Culture and Isolation

Golden shiner reovirus stock was purchased from ATCC (ATCC® VR957™) and was propagated in Fat Head Minnow cells (FHM; ATCC® CCL-42™) with a slight modification to previously described method (Shaw et al., 1996). FHM cells were cultured in MEM, hanks' balanced salts (Gibco™) supplemented with 10% fetal bovine serum (Atlanta biologicals), Penicillin (10,000 IU) and Streptomycin (10,000 µg/ml) (Corning ®, USA), and maintained at 28°C. Confluent monolayers of FHM were infected with ~5 plaque forming units of GSRV per cell for ~48 hours. Once cell syncytia was visible, media were collected from the infected cell culture and centrifuged at 11,000 g for 15 min to get rid of cells and cellular debris. Clean supernatant was centrifuged at 100,000g for 3 hours (SW28 rotors, Beckman Coulter) to pellet the viral particles. Supernatant was discarded and 100 µl of ice-chilled PBS buffer was added to each pellet to resuspend the viral particles overnight. Pellets were pooled and loaded on a 15%-50% sucrose gradient and banded by centrifuging at 100,000 g for 1 hour (SW41 rotor) at 4°C. Band containing the GCRV cores was harvested and diluted in PBS, pelleted at 100,000 g for 2 hours. The cores in the pellet were resuspended in PBS and quality confirmed by negative-staining (2% uranyl acetate) stain transmission electron microscopy.

CryoEM imaging

For cryoEM sample preparation, 2.5-µL aliquots of the GSRV core sample were applied to 200-mesh Quantifoil grid with 2µm-diameter hole size (2/2 or 2/1 Quantifoil) and plunge frozen in a Vitrobot Mark IV (Thermo Fisher Scientific) (Thermo Fisher Scientific) after blotting (blot time 15 seconds, blot force -5, 100% humidity and 4°C). Movies of dose fractionated image frames were recorded using a Titan Krios microscope (Thermo Fisher Scientific) equipped with a Gatan imaging filter (GIF) quantum LS and a post-GIF Gatan K2 Summit direct electron detector operated in super resolution mode at a nominal magnification of 105,000× yielding a calibrated

pixel size of 0.68 Å/pixel with SerialEM (Mastronarde, 2005). The GIF slit width was set to 20 eV at the zero-loss peak, and dose rate as recorded by the camera was set to with a total exposure dosage of ~45 e/Å^2 at the sample level which was fractionated equally into 40 frames. A defocus range of 1.5µm-2.5 µm was targeted for recordings. Dose-fractionated frames were binned 2× to (effective pixel size 1.36 Å) and aligned for beam induced motion correction to produce dose-weighted and unweighted micrographs, used for final reconstruction and initial screening and CTF estimation respectively, using MotionCor2 (Zheng et al., 2017). In total 12,258 movies were collected.

Data processing

Defocus values of the micrographs were initially estimated using CTFFIN4 (Rohou & Grigorieff, 2015), and those micrographs with significant ice contamination or defocus values beyond -0.8 and -3.0 µm were removed leaving 10,799 micrographs. 36,764 particles were initially selected by Ethan (Kivioja et al., 2000). The particles were extracted and were first subjected to an icosahedral refinement in RELION (Scheres, 2012). Asymmetric subparticle reconstructions were generated following the protocols previously described (Ding et al., 2018; Pan et al., 2021). Briefly, extracted ARV ICP particles were initially subjected icosahedral reconstruction in RELION (Scheres, 2013). This icosahedral reconstruction was used to guide the extraction of subparticles from around the I5 axes. The newly extracted subparticles were recentered further refined as new particles. Further symmetry expansion was performed along with focused classification to resolve the asymmetrically associated TECs from each of the 12 vertices. The vertices were sorted based on their polar or tropical localization and used to generate the asymmetric reconstruction of the polar and tropical vertices. The orientations determined during this process were subsequently applied to the complete capsid particles to create an asymmetric reconstruction of the entire viral particle.

Atomic Model Building and Refinement

Atomic models of the GSRV RdRp, CSP, NTPase, Turret and clamp proteins were initially modeled into the cryoEM density in Coot using the homologous proteins from the GCRV ISVP (Ascension number 6m99) (Emsley et al., 2010). Following initial fitting the polypeptide chains were mutated to match the GCRV sequence using Coot's Mutate Residue Range tool prior to local and global refinement in PHENIX (Afonine et al., 2018). Upon initial fitting the model was refined within the sub particle map using the Molecular dynamic flexible fitting feature of ISOLDE embedded within the UCSF ChimeraX program (Croll, 2018; Goddard et al., 2018). Models were then subjected to a final round of PHENIX real space refine and the resulting structure was validated by the worldwide protein data bank validation server (Afonine et al., 2018; Berman et al., 2003). Root mean squared deviations (RMSDs) between proteins were calculated using the matchmaker tool in UCSF ChimeraX. Internal capsid volume was calculated using the ChimeraX recipe "Measure volume enclosed by a virus capsid". TEC distribution maps were generated in UCSF Chimera (Pettersen et al., 2004).

Data Availability

CryoEM maps of the asymmetric GSRV ICP and subparticles have been submitted to the Electron Microscopy Data Bank and can be found under accession numbers EMD-XXXXX, EMD-XXXXX, EMD-XXXXX and EMD-XXXXX. The coordinates of ICP subparticle was deposited in the Protein Data Bank under accession number XXXX.

Figure Legends

Figure 1. Asymmetric reconstruction of ARV ICP. (A) CryoEM structures of ARV virion (left) (5VST) and ICP (right) with portion of their external layers removed along hemispheres to expose genome and TECs. (B) Table comparing volumetric difference between virion and ICP lumen. (C) Cross sectional view of Tropical Vertex featuring TEC and a turret. Layers of genome segments are numbered from 1-5 based on proximity to capsid wall. (D) ICP capsid decamer (top right) and VP3A (left) and VP3B (right) conformers with domains indicated and colored differently. (E) Position and orientation of the 11 ICP TECs relative to an icosahedron (grey) with Northern and Southern “poles” and “tropics” indicated. (F) Cross sectional view of ICP vertex without TEC showing that the TEC-free vertex is occupied by RNA density (yellow).

Figure 2. CryoEM maps two ICP vertices showing distinct arrangement of RNA and identical TEC structures. (A) Comparison of the CryoEM density maps from polar and tropical vertices, highlighting the TEC (magenta and cyan) and surrounding RNA, shown semi-transparently and superposed with corresponding dsRNA models (colored by segment). (B-H) Atomic model of ICP RdRp VP2 colored by domain, either shown together (B), or separately (D-H) for detailed features. (C) provides magnified view of catalytic palm domain from B and C, with catalytically important residues colored in white. In E and F views from D are shown to demonstrate the difference between the ICP and ISVP of the template channel finger loop (D) and catalytically important priming loop (F). (I) Atomic model of RdRp cofactor VP4 colored by domains with newly resolved residues indicated (red) and division of RBD into Main and Tip subdomains. (H) Interactions of the polar and charged residues from the newly resolved NTPase residues with the adjacent RNA segment from boxed region in A.

Figure 3. asymmetric interactions of $VP3_A$ N-termini with TEC and nucleic acids. (A and B) CryoEM map of polar decamer and attached TEC (left) with dimer pairs colored based on TEC association (A), and corresponding atomic model (B). Note the RNA is only shown in the atomic model (B) and not shown in the cryoEM density for clarity. (C) Superposition of $VP3_A$ proteins from each dimer pair, with N-terminal residues colored to match dimer pairs from A. (D) Depiction of TEC along decamer lumen with N-terminal surfaces of $VP3_A$ CSPs colored according to dimer pair in A (left), and hand shape added to improve visualization of Zn-fingers grasping TEC. (E-G) Side views of atomic model as indicated by eye symbols in B, with $VP3_A$ N-termini colored as in C (E and G), and magnified view of $VP3_{A3}$ Zn-finger domain interacting with both RdRp (magenta) and rear bottom dsRNA (cyan).

Figure 4. The novel conformational changes of the capping enzyme turret in uncoated virus. (A) comparison of CPV before and after detachment, where the Receptor binding spike remains attached to the turret and corresponding region of ARV virion and ICP. (B) Magnified view of turret pores from ARV virion (top) and ICP (bottom) with I5 symmetrical axis indicated with pentagon and line segment. (C) Atomic structure of the ARV turret protein VP1 from virion (left) and ICP (right) with superimposition of MTase domains (center) to show difference, with domains depicted (top) with the primary sequence number and corresponding color scheme. (D) magnified view of boxed region from C, with solid color of non-flap domains used to highlight virion to ICP differences.

Figure S1. Typical changes to Aquareovirus capsid during replciation. Diagrammatic representation of an Aquareovirus in cross section. The identities of viral structural and enzymatic proteins are indicated using the nomenclature for *Aquareoviruses* and assigned colors. Double-stranded DNA is represented by parallel blue line segments and single-stranded RNA is represented by orange lines.

Figure S2. Asymmetric reconstructions from ARV ICP. (A-C) CryoEM maps of GSRV ICP (A) and sub particles from Polar (B) and Tropical (C) vertices colored by local resolution. Internal views of Polar and Tropical vertices in B and C (right and middle panels respectively) showing the asymmetrically associated TEC in both species and the lack thereof in a subset of Tropical vertices (C, right).

Figure S3. Columbic potential maps of NTPase VP4. (A-C) different views of NTPase VP4 protein colored by domains (B-C, top). (B) view of NTPase as viewed along the opposite side of RdRp association with surface colored by columbic potential (bottom). (C) Provides a view of the RdRp associated side of NTPase in the same manner as B.

Movie S1. Expansion of ARV ICP decamer. Comparison of cryoEM maps and atomic models from core of ARV virion particle and ICP. Cartoon representation of ARV ICP, without TEC, conforming to same color scheme used in Fig. 1A. First morph movie demonstrates rise away from capsid center. Second morph toggles between virion and ICP decamers, superimposed at residues adjacent to the I5 vertices, from internal, side and external view to highlight conformational changes of capsid shell proteins (lime and red) and capping enzyme proteins (dark green). Rising motion away from virion origin not shown.

Movie S2. Local motion of CSP dimer from Virion to ICP. Cartoon representation of CSP dimer as colored in Fig. 1D, with local VP6 clamp proteins and the first 390 residues of the Turret protein VP1. Demonstrates local motion of VP3 monomers morphing between virion and ICP conformations. Side view demonstrates radial extension of $VP3_A$ and $VP3_B$ with the conserved position of $VP3_A$ α-helices 13 and 14. External view shows radial movement of clamp and turret proteins along external wall of ICP while their removal demonstrates the constrained movement of their interfaces during the morph.

Movie S3. Conformational changes from ISVP to ICP TEC. Cartoon representation of decamer and TEC morphs between ISVP and ICP, demonstrating asymmetric movement of TEC, with NTPase moving along with capsid lumen while the RdRp appears to expand, creating a breathing like motion. Movie also emphasizes changes to RdRp finger loop at template entry channel and priming loop retraction from the transcript exit channel.

Movie S4. Extension of Turret proteins. Cross-sectional view of ARV turret proteins morphing between virion and ICP structures along fixed CSPs from the ICP. Movie begins with virion turret proteins represented as surfaces morphing to ICP conformations.

References

Afonine, P. V., Poon, B. K., Read, R. J., Sobolev, O. V., Terwilliger, T. C., Urzhumtsev, A., & Adams, P. D. (2018). Real-space refinement in PHENIX for cryo-EM and crystallography. In *Acta Crystallographica Section D: Structural Biology* (Vol. 74, pp. 531-544): International Union of Crystallography.

Berman, H., Henrick, K., & Nakamura, H. (2003). Announcing the worldwide Protein Data Bank. In *Nature Structural & Molecular Biology* (Vol. 10, pp. 980-980).

Cheng, L., Fang, Q., Shah, S., Atanasov, I. C., & Zhou, Z. H. (2008). Subnanometer-Resolution Structures of the Grass Carp Reovirus Core and Virion. In *Journal of Molecular Biology* (Vol. 382, pp. 213-222).

Cheng, L., Sun, J., Zhang, K., Mou, Z., Huang, X., Ji, G., . . . Zhu, P. (2011). Atomic model of a cypovirus built from cryo-EM structure provides insight into the mechanism of mRNA capping. In *Proceedings of the National Academy of Sciences of the United States of America* (Vol. 108, pp. 1373-1378).

Croll, T. I. (2018). ISOLDE: A physically realistic environment for model building into low-resolution electron-density maps. In *Acta Crystallographica Section D: Structural Biology* (Vol. 74, pp. 519-530): International Union of Crystallography.

Cui, Y., Zhang, Y., Zhou, K., Sun, J., & Zhou, Z. H. (2019). Conservative transcription in three steps visualized in a double-stranded RNA virus. In *Nature Structural & Molecular Biology* (Vol. 26, pp. 1023-1034): Springer US.

Dai, X., Li, Z., Lai, M., Shu, S., Du, Y., Zhou, Z. H., & Sun, R. (2017). In situ structures of the genome and genome-delivery apparatus in a single-stranded RNA virus. In *Nature* (Vol. 541, pp. 112-116): Nature Publishing Group.

Decroly, E., Ferron, F., Lescar, J., & Canard, B. (2012). Conventional and unconventional mechanisms for capping viral mRNA. In *Nature Reviews Microbiology* (Vol. 10, pp. 51-65): Nature Publishing Group.

Ding, K., Celma, C. C., Zhang, X., Chang, T., Shen, W., Atanasov, I., . . . Zhou, Z. H. (2019). In situ structures of rotavirus polymerase in action and mechanism of mRNA transcription and release. In *Nature Communications* (Vol. 10, pp. 2216): Springer US.

Ding, K., Nguyen, L., & Zhou, Z. H. (2018). In Situ Structures of the Polymerase Complex and RNA Genome Show How Aquareovirus Transcription Machineries Respond to Uncoating. In S. López (Ed.), *Journal of Virology* (Vol. 92, pp. e00774-00718).

Dryden, K., Wang, G., Yeager, M., Nibert, M., Coombs, K., Furlong, D., . . . Baker, T. (1993). Early steps in reovirus infection are associated with dramatic changes in supramolecular structure and protein conformation: analysis of virions and subviral particles by cryoelectron microscopy and image reconstruction. In *Journal of Cell Biology* (Vol. 122, pp. 1023-1041).

Emsley, P., Lohkamp, B., Scott, W. G., & Cowtan, K. (2010). Features and development of Coot. In *Acta Crystallographica Section D Biological Crystallography* (Vol. 66, pp. 486-501): International Union of Crystallography.

Fang, Q., Shah, S., Liang, Y., & Zhou, Z. H. (2005). 3D reconstruction and capsid protein characterization of grass carp reovirus. In *Science in China, Series C: Life Sciences* (Vol. 48, pp. 593-600).

Farsetta, D. L., Chandran, K., & Nibert, M. L. (2000). Transcriptional Activities of Reovirus RNA Polymerase in Recoated Cores. In *Journal of Biological Chemistry* (Vol. 275, pp. 39693-39701): Â© 2000 ASBMB. Currently published by Elsevier Inc; originally published by American Society for Biochemistry and Molecular Biology.

Goddard, T. D., Huang, C. C., Meng, E. C., Pettersen, E. F., Couch, G. S., Morris, J. H., & Ferrin, T. E. (2018). UCSF ChimeraX: Meeting modern challenges in visualization and analysis. In *Protein Science* (Vol. 27, pp. 14-25).

He, Y., Shivakoti, S., Ding, K., Cui, Y., Roy, P., & Zhou, Z. H. (2019). In situ structures of RNA-dependent RNA polymerase inside bluetongue virus before and after uncoating. In *Proceedings of the National Academy of Sciences of the United States of America* (Vol. 116, pp. 16535-16540).

Kim, J., Tao, Y., Reinisch, K. M., Harrison, S. C., & Nibert, M. L. (2004). Orthoreovirus and Aquareovirus core proteins: conserved enzymatic surfaces, but not protein–protein interfaces. In *Virus Research* (Vol. 101, pp. 15-28).

Family - Reoviridae, Virus Taxonomy 541-637 (Elsevier 2012).

Kivioja, T., Ravantti, J., Verkhovsky, A., Ukkonen, E., & Bamford, D. (2000). Local average intensity-based method for identifying spherical particles in electron micrographs. In *Journal of structural biology* (Vol. 131, pp. 126-134).

Kumar, D., Yu, X., Crawford, S. E., Moreno, R., Jakana, J., Sankaran, B., . . . Prasad, B. V. V. (2020). 2.7 Å cryo-EM structure of rotavirus core protein VP3, a unique capping machine with a helicase activity. In *Science Advances* (Vol. 6, pp. 1-11).

Lemay, G., & Danis, C. (1994). Reovirus 1 Protein: Affinity for Double-stranded Nucleic Acids by a Small Amino-terminal Region of the Protein Independent From the Zinc Finger Motif. In *Journal of General Virology* (Vol. 75, pp. 3261-3266).

Luongo, C. L., Reinisch, K. M., Harrison, S. C., & Nibert, M. L. (2000). Identification of the guanylyltransferase region and active site in reovirus mRNA capping protein lambda2. In *The Journal of biological chemistry* (Vol. 275, pp. 2804-2810): Â© 2000 ASBMB. Currently published by Elsevier Inc; originally published by American Society for Biochemistry and Molecular Biology.

Mastronarde, D. N. (2005). Automated electron microscope tomography using robust prediction of specimen movements. In *Journal of Structural Biology* (Vol. 152, pp. 36-51).

McDonald, S. M., & Patton, J. T. (2011). Rotavirus VP2 Core Shell Regions Critical for Viral Polymerase Activation. In *Journal of Virology* (Vol. 85, pp. 3095-3105).

McEntire, M. E., Iwanowicz, L. R., & Goodwin, A. E. (2003). Molecular, physical, and clinical evidence that golden shiner virus and grass carp reovirus are variants of the same virus. In *Journal of Aquatic Animal Health* (Vol. 15, pp. 257-263).

Nason, E. L., Samal, S. K., & Venkataram Prasad, B. V. (2000). Trypsin-Induced Structural Transformation in Aquareovirus. In *Journal of Virology* (Vol. 74, pp. 6546-6555).

Pan, M., Alvarez-Cabrera, A. L., Kang, J. S., Wang, L., Fan, C., & Zhou, Z. H. (2021). Asymmetric reconstruction of mammalian reovirus reveals interactions among RNA, transcriptional factor μ2 and capsid proteins. In *Nature Communications* (Vol. 12, pp. 1-16): Springer US.

Parashar, U. D., Hummelman, E. G., Bresee, J. S., Miller, M. A., & Glass, R. I. (2003). Global Illness and Deaths Caused by Rotavirus Disease in Children. In *Emerging Infectious Diseases* (Vol. 9, pp. 565-572).

Pettersen, E. F., Goddard, T. D., Huang, C. C., Couch, G. S., Greenblatt, D. M., Meng, E. C., & Ferrin, T. E. (2004). UCSF Chimera-A visualization system for exploratory research and analysis. In *Journal of Computational Chemistry* (Vol. 25, pp. 1605-1612).

Reinisch, K. M., Nibert, M. L., & Harrison, S. C. (2000). Structure of the reovirus core at 3.6 Å resolution. In *Nature* (Vol. 404, pp. 960-967).

Rohou, A., & Grigorieff, N. (2015). CTFFIND4: Fast and accurate defocus estimation from electron micrographs. In *Journal of Structural Biology* (Vol. 192, pp. 216-221): Elsevier Inc.

Scheres, S. H. W. (2013). Single-particle processing in RELION. In *Manuals* (pp. 1-21).

Shaw, A. L., Samal, S. K., Subramanian, K., & Prasad, B. V. (1996). The structure of aquareovirus shows how the different geometries of the two layers of the capsid are reconciled to provide symmetrical interactions and stabilization. In *Structure* (Vol. 4, pp. 957-967).

Skehel, J. J., & Joklik, W. K. (1969). Studies on the in vitro transcription of reovirus RNA catalyzed by reovirus cores. In *Virology* (Vol. 39, pp. 822-831).

Wang, X., Zhang, F., Su, R., Li, X., Chen, W., Chen, Q., . . . Cheng, L. (2018). Structure of RNA polymerase complex and genome within a dsRNA virus provides insights into the mechanisms of transcription and assembly. In *Proceedings of the National Academy of Sciences of the United States of America* (Vol. 115, pp. 7344-7349).

Yang, C., Ji, G., Liu, H., Zhang, K., Liu, G., Sun, F., . . . Cheng, L. (2012). Cryo-EM structure of a transcribing cypovirus. In *Proceedings of the National Academy of Sciences of the United States of America* (Vol. 109, pp. 6118-6123).

Yu, X., Ge, P., Jiang, J., Atanasov, I., & Zhou, Z. H. (2011). Atomic Model of CPV Reveals the Mechanism Used by This Single-Shelled Virus to Economically Carry Out Functions Conserved in Multishelled Reoviruses. In *Structure* (Vol. 19, pp. 652-661): Elsevier Ltd.

Yu, X., Jiang, J., Sun, J., & Zhou, Z. H. (2015). A putative ATPase mediates RNA transcription and capping in a dsRNA virus. In *eLife* (Vol. 4, pp. e07901).

Zhang, X., Ding, K., Yu, X., Chang, W., Sun, J., Zhou, Z. H., & Hong Zhou, Z. (2015). In situ structures of the segmented genome and RNA polymerase complex inside a dsRNA virus. In *Nature* (Vol. 527, pp. 531-534): Nature Publishing Group.

Zhang, X., Ji, Y., Zhang, L., Harrison, S. C., Marinescu, D. C., Nibert, M. L., & Baker, T. S. (2005). Features of Reovirus Outer Capsid Protein μ1 Revealed by Electron Cryomicroscopy and Image Reconstruction of the Virion at 7.0 Å Resolution. In *Structure* (Vol. 13, pp. 1545-1557).

Zhang, X., Jin, L., Fang, Q., Hui, W. H., & Zhou, Z. H. (2010). 3.3 Å Cryo-EM Structure of a Nonenveloped Virus Reveals a Priming Mechanism for Cell Entry. In *Cell* (Vol. 141, pp. 472-482).

Zhang, Y., Cui, Y., Sun, J., & Zhou, Z. H. (2022). Multiple conformations of trimeric spikes visualized on a non-enveloped virus. In *Nature Communications* (Vol. 13, pp. 550): Springer US.

Zheng, S. Q., Palovcak, E., Armache, J.-P., Verba, K. A., Cheng, Y., & Agard, D. A. (2017). MotionCor2: anisotropic correction of beam-induced motion for improved cryo-electron microscopy. In *Nature Methods* (Vol. 14, pp. 331-332).

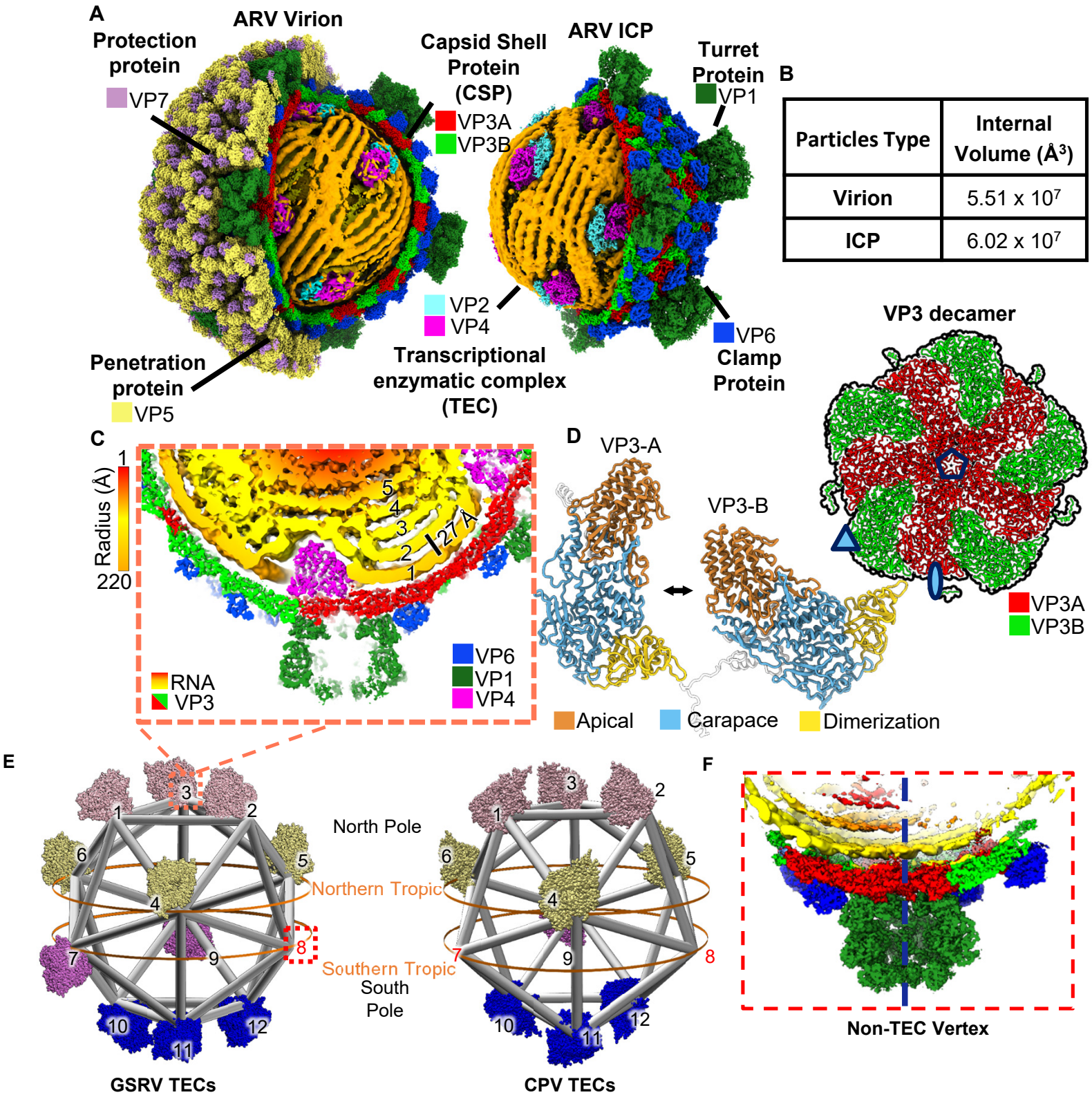

Particles Type	Internal Volume (Å^3)
Virion	5.51 x 10^7
ICP	6.02 x 10^7

Figure 1. Asymmetric reconstruction of ARV ICP. (A) CryoEM structures of ARV virion (left) (5VST) and ICP (right) with portion of their external layers removed along hemispheres to expose genome and TECs. (B) Table comparing volumetric difference between virion and ICP lumen. (C) Cross sectional view of Tropical Vertex featuring TEC and a turret. Layers of genome segments are numbered from 1-5 based on proximity to capsid wall. (D) ICP capsid decamer (top right) and VP3A (left) and VP3B (right) conformers with domains indicated and colored differently. (E) Position and orientation of the 11 ICP TECs relative to an icosahedron (grey) with Northern and Southern "poles" and "tropics" indicated. (F) Cross sectional view of ICP vertex without TEC showing that the TEC-free vertex is occupied by RNA density (yellow).

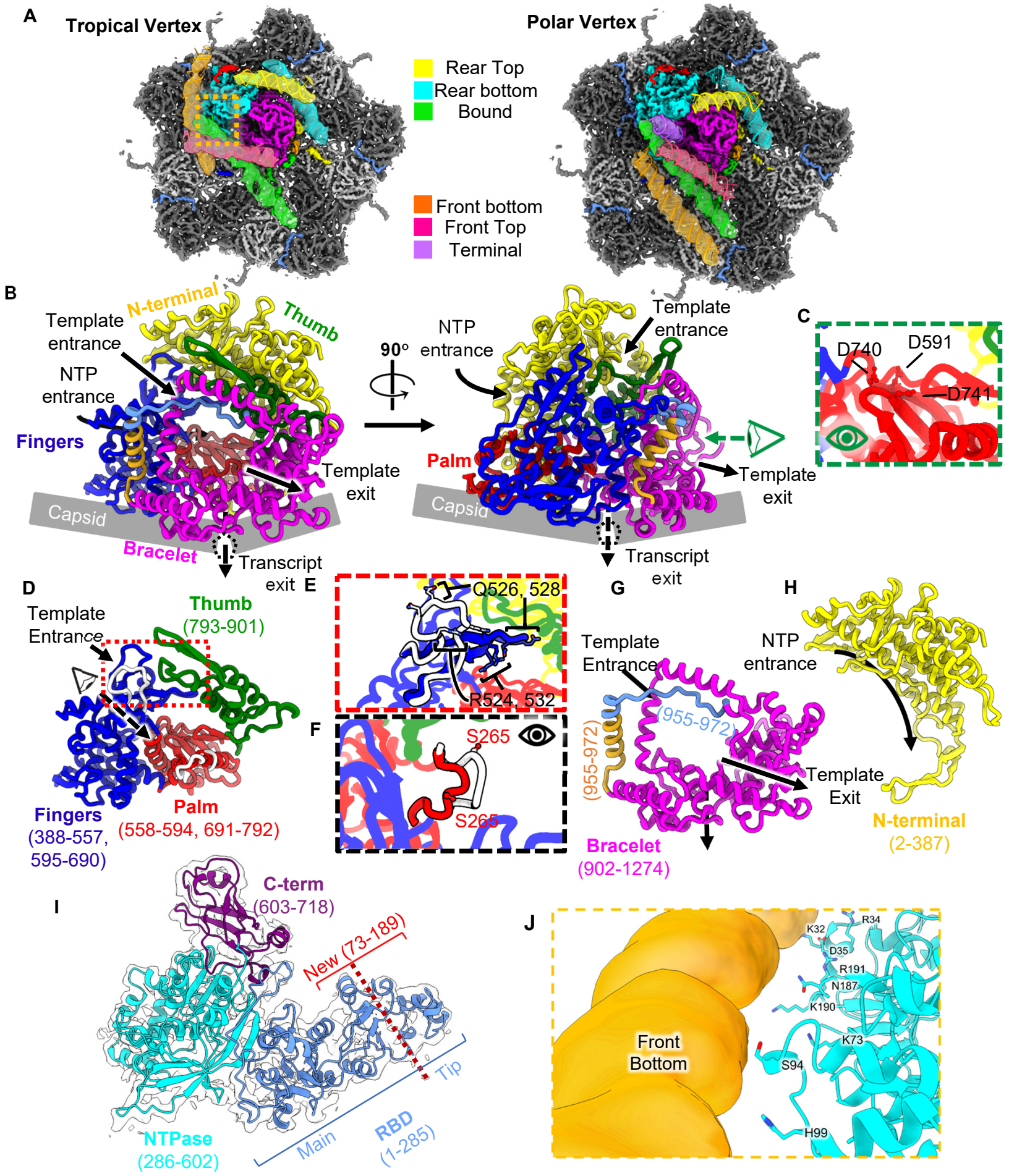
A
Tropical Vertex
Polar Vertex
Rear Top
Rear bottom
Bound
Front bottom
Front Top
Terminal
B
N-terminal
Thumb
Template entrance
NTP entrance
Fingers
Template exit
Capsid
Bracelet
Transcript exit
90°
NTP entrance
Template entrance
Palm
Template exit
Capsid
Transcript exit
C
D740
D591
D741
D
Template Entrance
Thumb (793-901)
Fingers (388-557, 595-690)
Palm (558-594, 691-792)
E
Q526, 528
R524, 532
F
S265
S265
G
Template Entrance
(955-972)
(955-972)
Template Exit
Bracelet (902-1274)
H
NTP entrance
N-terminal (2-387)
I
C-term (603-718)
New (73-189)
Tip
Main
RBD (1-285)
NTPase (286-602)
J
K32
R34
D35
R191
N187
K190
K73
S94
H99
Front Bottom

Figure 2. CryoEM maps two ICP vertices showing distinct arrangement of RNA and identical TEC structures. (A) Comparison of the CryoEM density maps from polar and tropical vertices, highlighting the TEC (magenta and cyan) and surrounding RNA, shown semi-transparently and superposed with corresponding dsRNA models (colored by segment). (B-H) Atomic model of ICP RdRp VP2 colored by domain, either shown together (B), or separately (D-H) for detailed features. (C) provides magnified view of catalytic palm domain from B and C, with catalytically important residues colored in white. In E and F views from D are shown to demonstrate the difference between the ICP and ISVP of the template channel finger loop (D) and catalytically important priming loop (F). (I) Atomic model of RdRp cofactor VP4 colored by domains with newly resolved residues indicated (red) and division of RBD into Main and Tip subdomains. (H) Interactions of the polar and charged residues from the newly resolved NTPase residues with the adjacent RNA segment from boxed region in A.

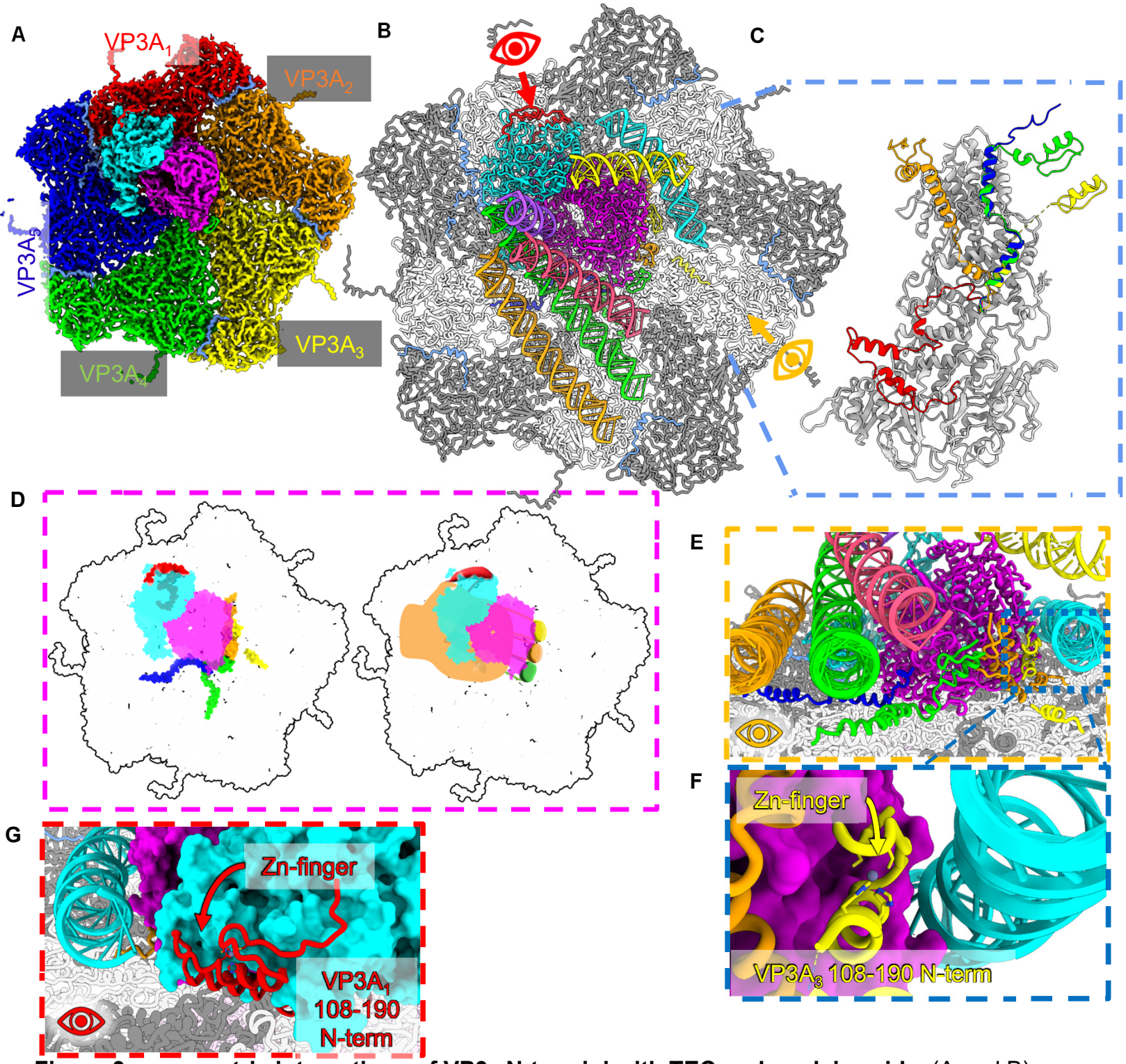

Figure 3. asymmetric interactions of $VP3_A$ N-termini with TEC and nucleic acids. (A and B) CryoEM map of polar decamer and attached TEC (left) with dimer pairs colored based on TEC association (A), and corresponding atomic model (B). Note the RNA is only shown in the atomic model (B) and not shown in the cryoEM density for clarity. (C) Superposition of $VP3_A$ proteins from each dimer pair, with N-terminal residues colored to match dimer pairs from A. (D) Depiction of TEC along decamer lumen with N-terminal surfaces of $VP3_A$ CSPs colored according to dimer pair in A (left), and hand shape added to improve visualization of Zn-fingers grasping TEC. (E-G) Side views of atomic model as indicated by eye symbols in B, with $VP3_A$ N-termini colored as in C (E and G), and magnified view of $VP3_{A3}$ Zn-finger domain interacting with both RdRp (magenta) and rear bottom dsRNA (cyan).

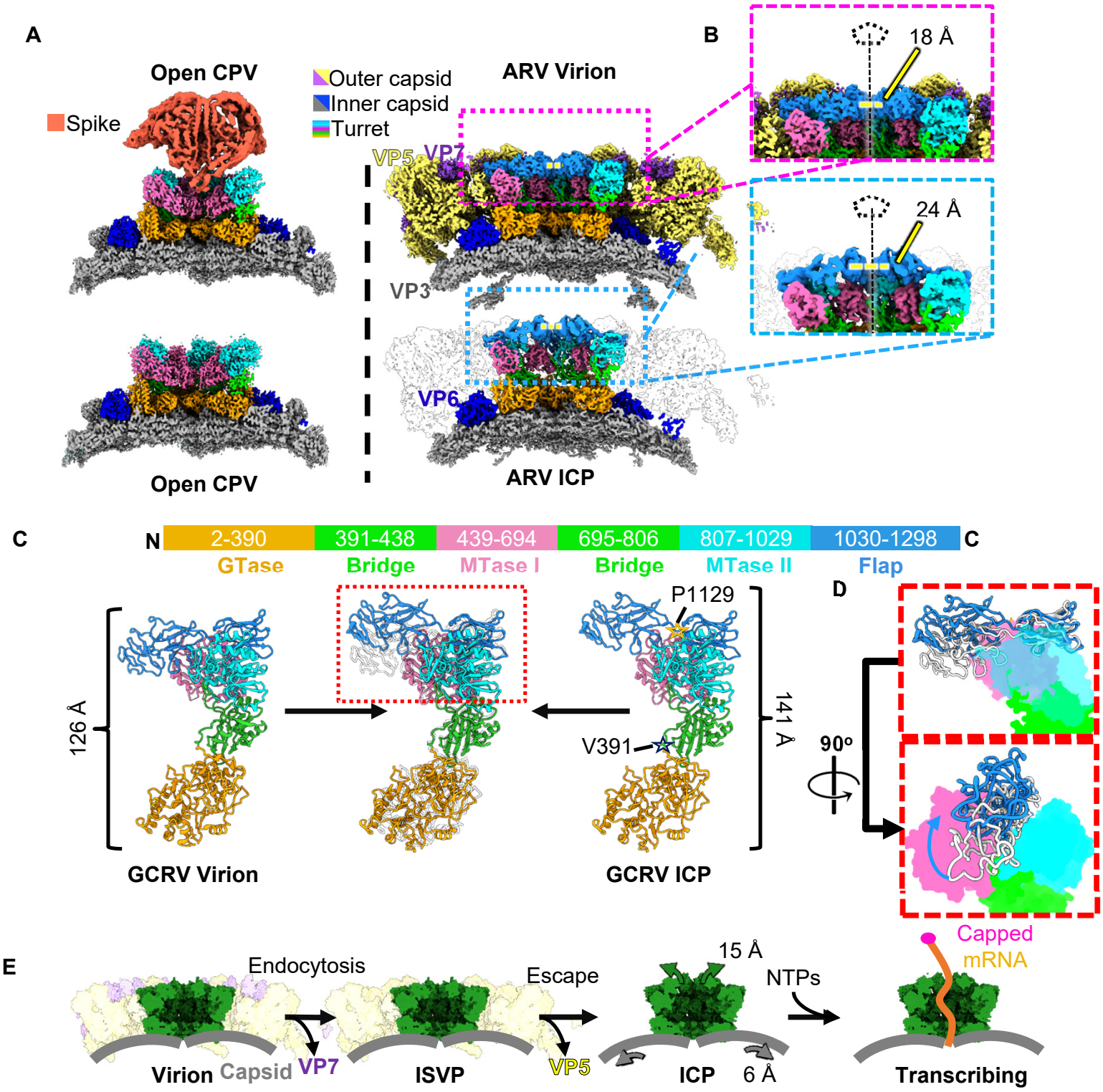

Figure 4. The novel conformational changes of the capping enzyme turret in uncoated virus. (A) comparison of CPV before and after detachment, where the Receptor binding spike remains attached to the turret and corresponding region of ARV virion and ICP. (B) Magnified view of turret pores from ARV virion (top) and ICP (bottom) with I5 symmetrical axis indicated with pentagon and line segment. (C) Atomic structure of the ARV turret protein VP1 from virion (left) and ICP (right) with superimposition of MTase domains (center) to show difference, with domains depicted (top) with the primary sequence number and corresponding color scheme. (D) magnified view of boxed region from C, with solid color of non-flap domains used to highlight virion to ICP differences.

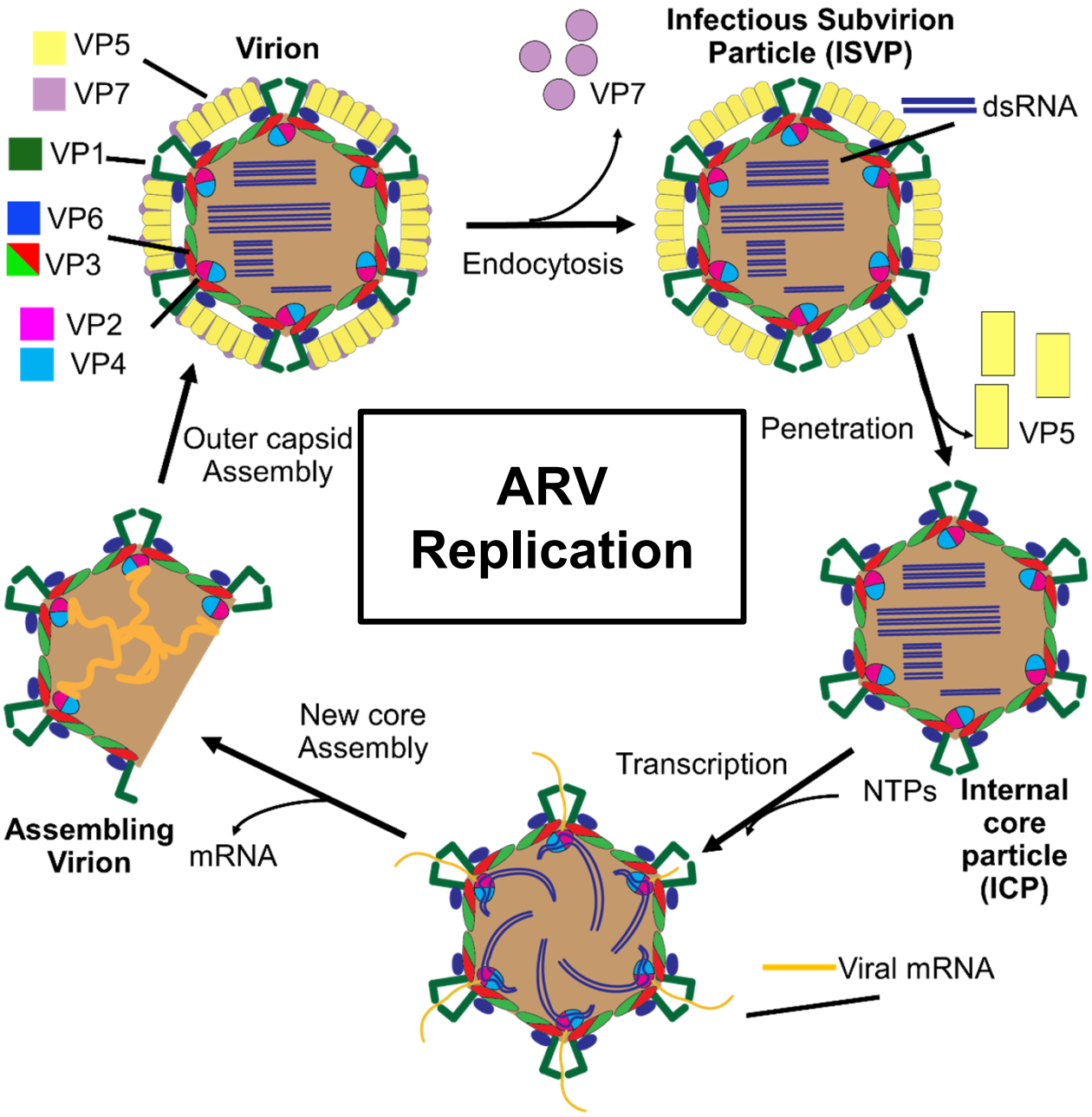

Figure S1. Typical changes to Aquareovirus capsid during replciation. Diagrammatic representation of an Aquareovirus in cross section. The identities of viral structural and enzymatic proteins are indicated using the nomenclature for *Aquareoviruses* and assigned colors. Double-stranded DNA is represented by parallel blue line segments and single-stranded RNA is represented by orange lines.

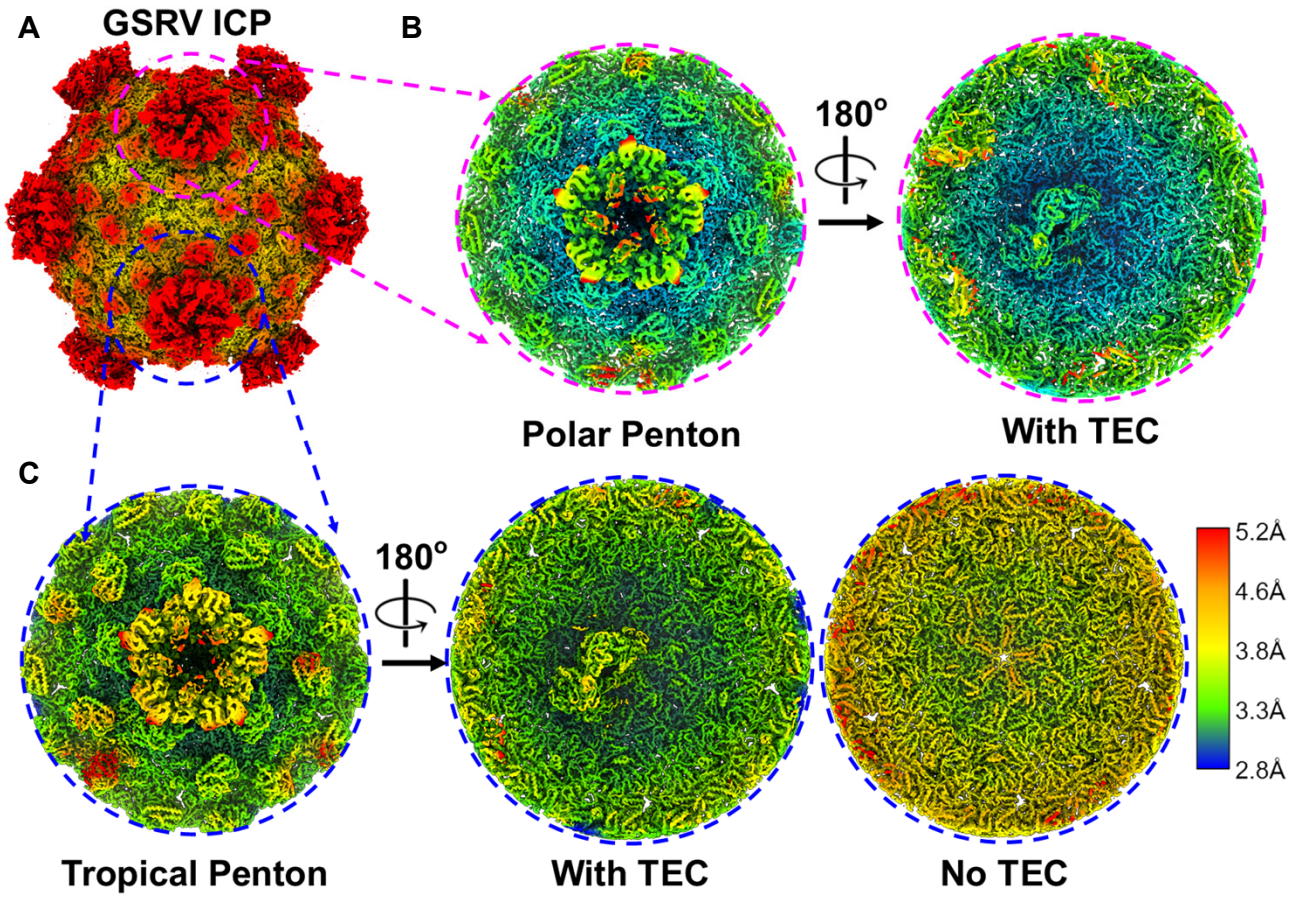

Figure S2. Asymmetric reconstructions from ARV ICP. (A-C) CryoEM maps of GSRV ICP (A) and sub particles from Polar (B) and Tropical (C) vertices colored by local resolution. Internal views of Polar and Tropical vertices in B and C (right and middle panels respectively) showing the asymmetrically associated TEC in both species and the lack thereof in a subset of Tropical vertices (C, right).

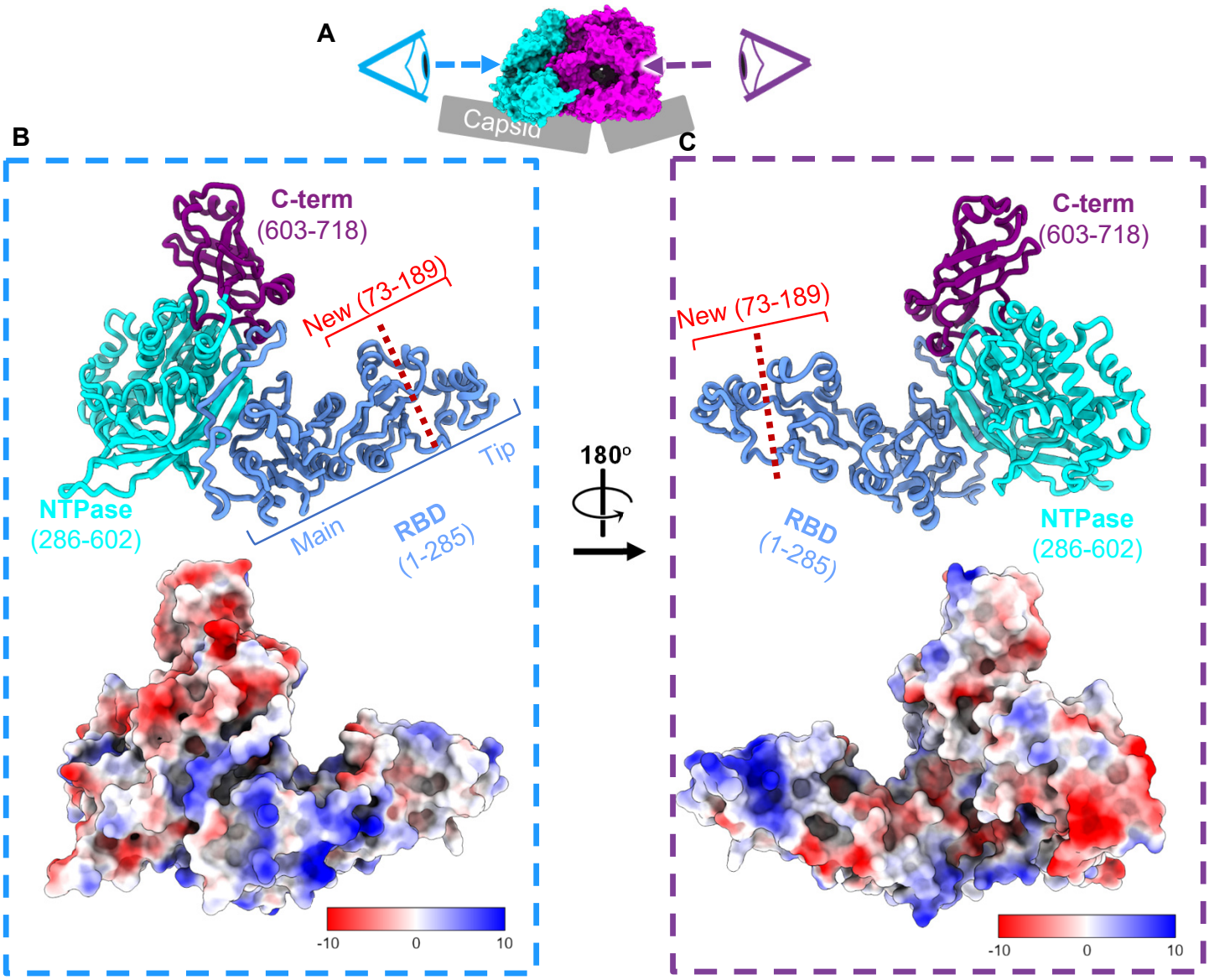

Figure S3. Columbic potential maps of NTPase VP4. (A-C) different views of NTPase VP4 protein colored by domains (B-C, top). (B) view of NTPase as viewed along the opposite side of RdRp association with surface colored by columbic potential (bottom). (C) Provides a view of the RdRp associated side of NTPase in the same manner as B.

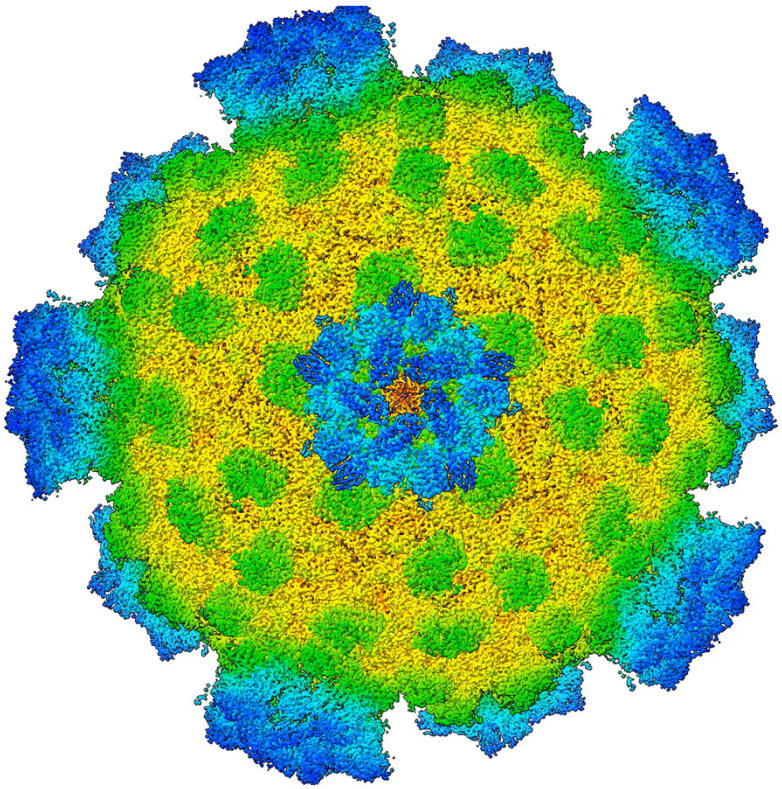

Movie S1. Expansion of ARV ICP decamer. Comparison of cryoEM maps and atomic models from core of ARV virion particle and ICP. Cartoon representation of ARV ICP, without TEC, conforming to same color scheme used in Fig. 1A. First morph movie demonstrates rise away from capsid center. Second morph toggles between virion and ICP decamers, superimposed at residues adjacent to the I5 vertices, from internal, side and external view to highlight conformational changes of capsid shell proteins (lime and red) and capping enzyme proteins (dark green). Rising motion away from virion origin not shown.

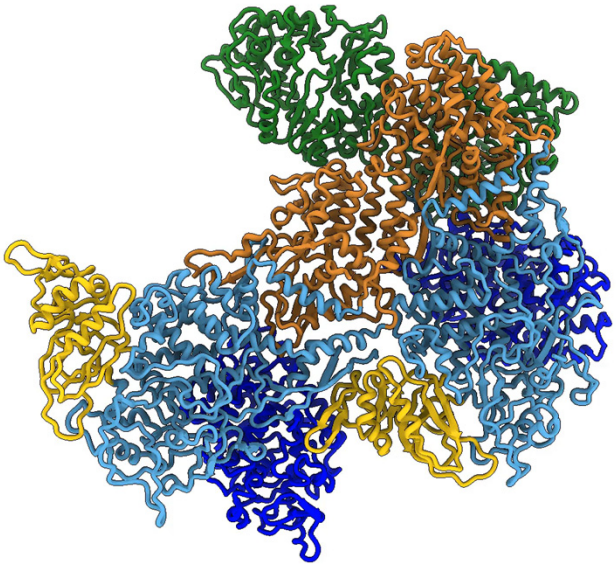

Movie S2. Local motion of CSP dimer from Virion to ICP. Cartoon representation of CSP dimer as colored in Fig. 1D, with local VP6 clamp proteins and the first 390 residues of the Turret protein VP1. Demonstrates local motion of VP3 monomers morphing between virion and ICP conformations. Side view demonstrates radial extension of $VP3_A$ and $VP3_B$ with the conserved position of $VP3_A$ α-helices 13 and 14. External view shows radial movement of clamp and turret proteins along external wall of ICP while their removal demonstrates the constrained movement of their interfaces during the morph.

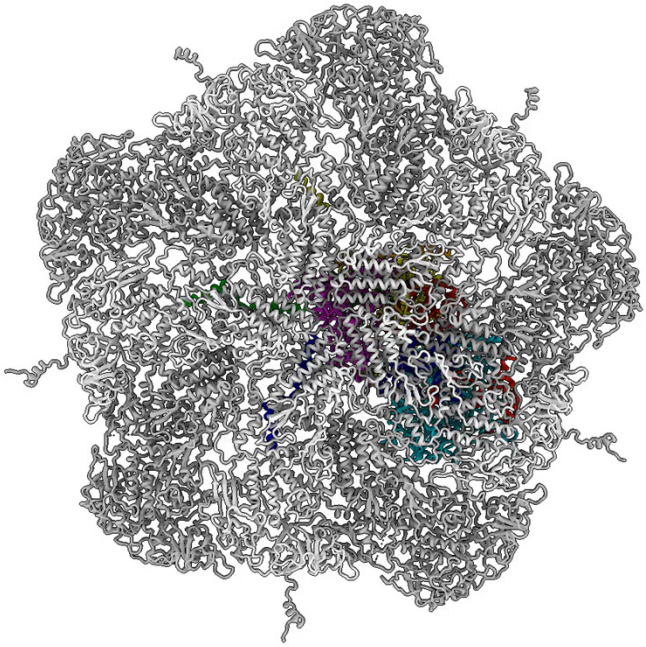

Movie S3. Conformational changes from ISVP to ICP TEC. Cartoon representation of decamer and TEC morphs between ISVP and ICP, demonstrating asymmetric movement of TEC, with NTPase moving along with capsid lumen while the RdRp appears to expand, creating a breathing like motion. Movie also emphasizes changes to RdRp finger loop at template entry channel and priming loop retraction from the transcript exit channel.

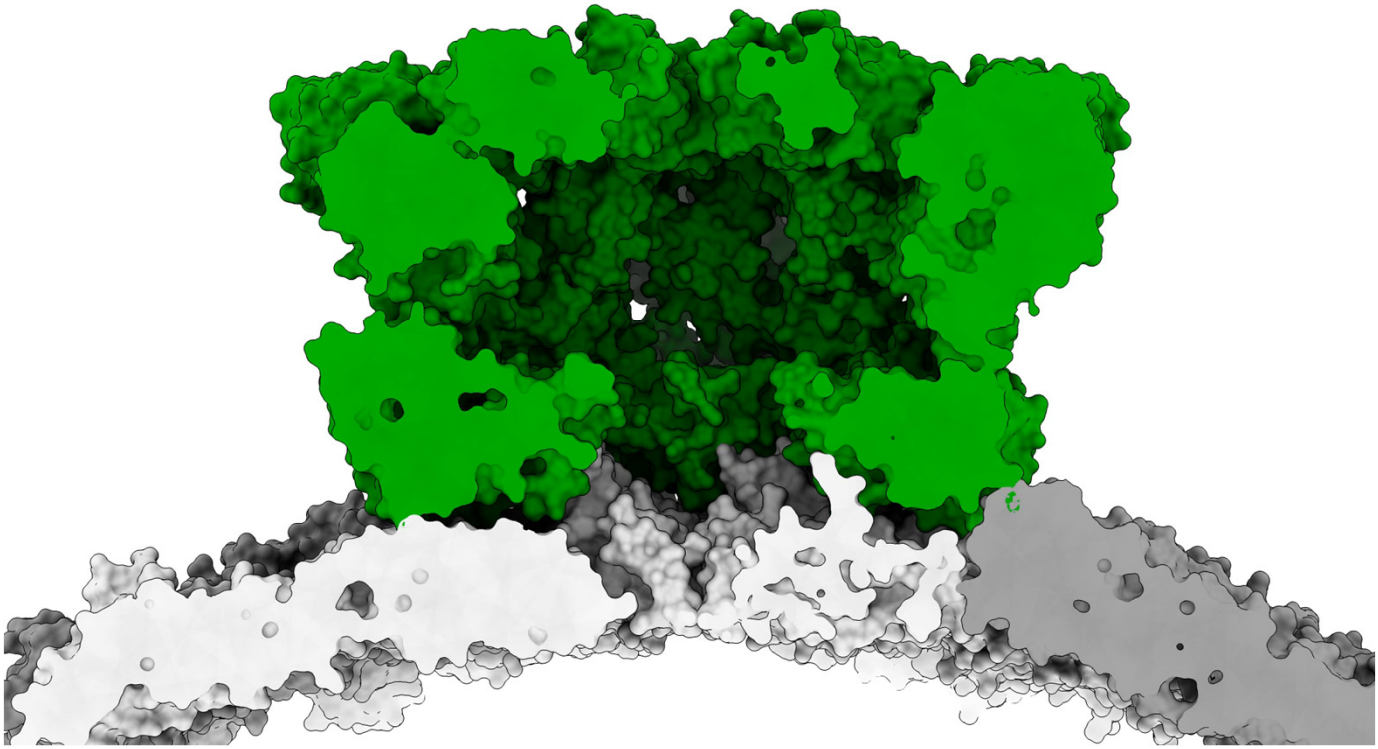

Movie S4. Extension of Turret proteins. Cross-sectional view of ARV turret proteins morphing between virion and ICP structures along fixed CSPs from the ICP. Movie begins with virion turret proteins represented as surfaces morphing to ICP conformations.